frontiers | Frontiers in Remote Sensing

TYPE Original Research
PUBLISHED 11 December 2024
DOI 10.3389/frsen.2024.1495958

OPEN ACCESS

EDITED BY
Vittorio Ernesto Brando,
National Research Council (CNR), Italy

REVIEWED BY
Elisabetta Canuti,
Joint Research Centre, Italy
Lingqi Ma,
Xiamen University, China

*CORRESPONDENCE
Robert J. W. Brewin,
r.brewin@exeter.ac.uk

RECEIVED 13 September 2024
ACCEPTED 25 November 2024
PUBLISHED 11 December 2024

CITATION
Tanner EP, Ewin H, Viljoen JJ and Brewin RJW (2024) Revisiting the relationship between surface and column-integrated chlorophyll-*a* concentrations in the Biogeochemical-Argo and satellite era.
Front. Remote Sens. 5:1495958.
doi: 10.3389/frsen.2024.1495958

Revisiting the relationship between surface and column-integrated chlorophyll-*a* concentrations in the Biogeochemical-Argo and satellite era

Ella Poppy Tanner, Harry Ewin, Johannes J. Viljoen and Robert J. W. Brewin*

Centre for Geography and Environmental Science, University of Exeter, Penryn, Cornwall, United Kingdom

Phytoplankton occupy the oceans' euphotic zone and are responsible for its primary production; thus, our ability to monitor their patterns of abundance and physiology is vital for tracking ocean health. Ocean colour sensors mounted on satellites can monitor the surface patterns of phytoplankton daily at global scales but cannot see into the subsurface. Autonomous robotic platforms, like Biogeochemical-Argo (BGC-Argo) profiling floats, do not have the coverage of satellites but can monitor the subsurface. Combining these methods can help track phytoplankton patterns throughout the euphotic zone. In this study, using a global array of BGC-Argo floats (76,043 profiles, spanning from 2010 to 2023), we revisit empirical relationships between the surface and column-integrated concentrations of chlorophyll-*a* (a proxy for phytoplankton abundance and physiology), originally developed using ship-based profiling data. We show that these relationships agree well with BGC-Argo float data. We then extend the relationships, removing the binary switch in parameters between mixed and stratified waters and trophic conditions such that the column-integrated chlorophyll-*a* concentration can be estimated as a continuous function of surface chlorophyll-*a* and a proxy for stratification (we use the optical mixed-layer depth, the mixed-layer depth multiplied by the diffuse attenuation coefficient, which is proportional to the ratio of the euphotic depth to the mixed layer depth when it approaches 1). The new model is shown to perform well in statistical tests (using separate training and independent validation data, with a correlation coefficient >0.73) and has fewer parameters than the earlier version. The model can be applied to satellite observations of surface chlorophyll-*a* and diffuse attenuation, together with fields of mixed-layer depth (e.g., from Argo), to track changes in column-integrated chlorophyll-*a*. Such fields may be useful for obtaining estimates of primary production, evaluating ecosystem models, and quantifying trophic energy transfer. The model may also be used to evaluate the influence of changing stratification patterns on phytoplankton abundance and physiology.

KEYWORDS

phytoplankton, BGC-Argo, vertical structure, global, ocean colour, chlorophyll-*a*

1 Introduction

Phytoplankton are primary producers found in the ocean that contribute to carbon sequestration. Since their origin over two billion years ago, phytoplankton have had a profound influence on Earth's biogeochemistry (Falkowski et al., 2003). Although their biomass only accounts for 1%–2% of the global total, they contribute around 50% of the global net primary production (Longhurst et al., 1995; Field et al., 1998). This primary production plays a central role in the ocean biological carbon pump, which transfers carbon from the surface to the deep ocean, where it can be stored for centuries (Boyd et al., 2019; Nowicki et al., 2022). This uptake and storage of atmospheric carbon dioxide (CO_2) helps control the global climate (Falkowski, 1994; Legendre and Rassoulzadgan, 1996). Phytoplankton also represent the foundation of oceanic food webs and are responsible for providing the energy that maintains the pelagic ecosystem. Phytoplankton production is closely coupled with the biomass and health of pelagic fish and other marine life (Kiørboe, 1993). As phytoplankton get eaten by consumers, carbon, energy, and other substances they contain are propagated to the upper trophic levels with relatively constant efficiency (Barnes et al., 2010).

In recent years, many changes have been observed in the abundance, physiology, and community composition of phytoplankton, caused by climate variability, ocean warming, shifts in ocean stratification, increasing numbers of extreme events, and eutrophication (Ardyna et al., 2014; Cheng et al., 2019; Dai et al., 2023; Deppeler and Davidson, 2017; Ferreira et al., 2022; Lu et al., 2022; Xiao et al., 2018; Sridevi et al., 2019; Trainer et al., 2020; Wang et al., 2021; 2022). Considering the profound impact phytoplankton have on ocean biogeochemical cycles and food webs, and considering current uncertainty in climate projections (IPCC, 2021), tracking the abundance and physiology of marine phytoplankton is of high importance. The chlorophyll-*a* concentration (Chl-*a*), a photosynthetic pigment present in one form or another in all marine phytoplankton, can be used to monitor phytoplankton abundance and physiology because it can be measured relatively easily through optical sensors mounted on satellites or *in situ* autonomous platforms and ship-based profiling rigs.

Satellites can observe the colour of the surface ocean remotely with high spatial coverage and temporal frequency and use changes in its colour to infer Chl-*a* concentrations (Groom et al., 2019). Satellite-observed ocean colour has provided oceanographers data to monitor temporal and spatial trends in Chl-*a* at global and regional scales (Garnesson et al., 2019; Le Traon et al., 2015; McClain et al., 2004). It is thought that by 2029, the ocean colour record will be long enough to discriminate between the effects of climate change and natural variability on phytoplankton (Groom et al., 2019), although some work has suggested that we have already reached this point (Cael et al., 2023). Yet, satellite remote sensing of ocean colour can only observe the surface layer of the ocean (typically < 40 m), and phytoplankton features below this level, such as deep chlorophyll maxima (DCM) common in stratified regions (Cullen, 2015) and capable of contributing significantly to stocks and fluxes of phytoplankton of carbon (Brewin et al., 2022; Cox et al., 2023; Ma et al., 2023; Viljoen et al., 2024), are missed. Consequently, water-column stocks of Chl-*a* cannot be directly measured by the passive satellite ocean colour.

Historically, ship-based methods were used to collect critical data on phytoplankton in deeper layers of the euphotic zone (sunlit region of the ocean) using profiling rigs equipped with bottles for water sampling or *in vivo* fluorometic sensors. However, the sparsity of ship-based sampling meant that these observations were not useful for monitoring phytoplankton over large spatial scales (e.g., global). One solution to this issue was to use ship-based sampling to establish empirical relationships between surface Chl-*a* concentrations and column-integrated concentrations within the euphotic zone (Morel and Berthon, 1989; Uitz et al., 2006). These empirical relationships could then be used with surface Chl-*a* concentrations from satellite remote sensing of ocean colour to predict global stocks of Chl-*a* pigment concentrations. These empirical relationships have proven useful for estimating phytoplankton stocks globally and quantifying energy transfer and biomass of higher trophic levels (e.g., Hatton et al., 2021). Yet, these relationships were developed using relatively few vertical profiles (Morel and Berthon, 1989; Uitz et al., 2006) and switch parametrisations, in a binary manner, between environmental (stratified or well-mixed waters) and trophic conditions.

Over the past few decades, increasing numbers of autonomous profiling floats have been deployed at a global scale to increase the vertical profiling of the ocean (Chai et al., 2020; Claustre et al., 2020), providing real-time and delayed-mode calibrated data that are freely available (Gould et al., 2013; Roemmich et al., 2009). The core Argo floats collect physical ocean data from which variables such as mixed-layer depth (MLD) can be calculated (Oka et al., 2007). More recently, the Biogeochemical-Argo (BGC-Argo) programme includes a network of floats holding additional sensors that observe biogeochemical properties such as Chl-*a* and particulate backscattering (Claustre et al., 2020). These profiling floats have significantly expanded the number and distribution of vertical profiles of Chl-*a* in the ocean, filling gaps in ocean observations at global and regional scales (Claustre et al., 2020; Jayne et al., 2017; Mignot et al., 2014).

In this paper, we use vertical profiles of Chl-*a* collected using the global network of BGC-Argo floats to revisit empirical relationships between surface and column-integrated Chl-*a* concentrations within the euphotic zone, developed by Morel and Berthon (1989) and Uitz et al. (2006). We then explore whether these relationships can be refined to produce a more parsimonious relationship, not dependent on a binary classification of physical and trophic conditions, with a view to improve our ability to estimate stocks of phytoplankton Chl-*a* concentration in the euphotic zone from satellite remote sensing.

2 Methods

2.1 Study area—the global ocean

In line with the studies by Morel and Berthon (1989) and Uitz et al. (2006), our work focused on the global ocean. Consequently, we needed a dataset representative of all oceans. Our dataset needed to include high-productivity regions commonly found in upwelling zones such as some coastal waters, around the equator, and at high latitudes due to an abundance of nutrients in the euphotic zone (Lalli and Parsons, 1997). Additionally, data from the large subtropical gyres were required, known for their extremely low productivity as a

result of nutrient limitations and the presence of DCMs (Miller, 2004). Our dataset also needed to cover high-nutrient low-chlorophyll (HNLC) regions, such as the Southern Ocean, with high levels of nutrients but low phytoplankton biomass (Le Moigne et al., 2013; Sergi et al., 2020), due to a range of limiting variables including the supply of micronutrients, principally iron (Ardyna et al., 2017; Bazzani et al., 2023; Strzedek et al., 2019).

2.2 Data collection

2.2.1 A global BGC-Argo dataset

Global BGC-Argo float data (synthetic files; S-prof) were downloaded on 28 November 2023 from the Argo Global Data Assembly Centre (GDAC) using a customised Python functions from the GO-BGC float toolbox (https://www.go-bgc.org/getting-started-with-go-bgc-data) that are available on GitHub (https://github.com/go-bgc/workshop-python). The function was adapted to download data from all global BGC-Argo floats equipped with sensors for both Chl-*a* fluorescence and particulate backscattering. The resulting dataset included data from 922 BGC-Argo floats, which operated between 30 May 2010 and 27 November 2023.

All floats were equipped with sensors collecting data on pressure (dBar, approximately proportional to the depth in metres); temperature (°C); salinity (PSU); Chl-*a* (mg m^{-3}); and backscattering by particles (at a wavelength of 700 nm, m^{-1}) at each profile location, with some also containing measurements of downwelling irradiance (photosynthetically active radiation [PAR], μmol photons m^{-2} s^{-1}). All profiles included a quenching correction for Chl-*a*-adjusted profiles and a standardising adjustment for pressure to facilitate work between core-Argo and BGC-Argo variables (Bittig et al., 2019; Schmechtig et al., 2023).

The original dataset, representative of all ocean basins, contained 130,354 profiles. For each profile, the following metrics were computed: (1) surface Chl-*a* (C_{surf}) was computed as the median of Chl-*a* in the top 10 m of the water column (typically within the mixed-layer; Boyer Montégut et al., 2004); (2) diffuse attenuation coefficient (K_d) was computed by fitting a Beer–Lambert law to PAR and pressure data in the top 100 m of the water column if PAR was present in float data. If PAR was not present, K_d was estimated from C_{surf} using the method suggested by Morel et al. (2007) by estimating the euphotic depth and dividing 4.6 by it; (3) euphotic depth (Z_p) was estimated by dividing 4.6 by K_d; (4) mixed-layer depth (Z_m) was computed from temperature profiles, using the methods suggested by Boyer Montégut et al. (2004); (5) optical mixed-layer depth, K_{zm}, was estimated by multiplying K_d by Z_m; (6) column-integrated Chl-*a* (C_{int}) in the euphotic zone [defined as $1.5 \times Z_p$, following Uitz et al. (2006)] was estimated using trapezoid integration; (7) surface particulate backscattering ($b_{bp,surf}$) was computed as the median of b_{bp} in the top 10 m of the water column; and (8) column-integrated particulate backscattering ($b_{bp,\mathrm{int}}$) in the euphotic ($1.5 \times Z_p$) zone was estimated using trapezoid integration.

These data were then cleaned first by using the Argo's QC-assigned numbers for Chl-*a* and b_{bp} profiles (profiles with median values above 2 were removed) and removing data that fell outside certain bounds. Latitude (degrees) and longitude (degrees) had to fall between −90 and 90 and −180 and 180, respectively, the geographical bounds of the planet. K_d (m^{-1}) had to fall between 0.02 (close to the theoretical limit of pure water) and 3 (at the extreme high end in the ocean), and Z_m (m) had to vary between 10 [near-surface value of temperature defined using the method suggested by Boyer Montégut et al. (2004)] and 4,000 (an extremely high end in the ocean). Similarly, C_{surf} ($0.01 < \mathrm{mg\ m^{-3}} > 20$), C_{int} ($0.01 < \mathrm{mg\ m^{-2}} > 1{,}000$), $b_{bp,surf}$ ($10^{-6} < \mathrm{m^{-1}} > 0.01$), and $b_{bp,\mathrm{int}}$ ($10^{-6} < b_{bp,\mathrm{int}} > 10$) all had to fall between low and high values, set at the very extreme ends of reality, to remove any grossly unrealistic values. This left 76,043 profiles, as shown in Figure 1.

2.2.2 Satellite data

Global satellite climatology data, at a spatial resolution of 9 km (mapped, level-3 products) and at a temporal resolution of season, were downloaded from NASA's Ocean Colour data assembly centre (NASA, 2022). The data were collected by the Moderate Resolution Imaging Spectroradiometer (MODIS) sensor on the Aqua satellite. Two products were downloaded, Chl-*a* concentration (surface) and diffuse attenuation coefficient at 490 nm [converted to the diffuse attenuation coefficient of PAR, following Morel et al. (2007)], for the four seasons.

2.2.3 Mixed-layer depth climatology

Global monthly maps of mixed-layer depth (Z_m) at a lateral resolution of 0.5° were downloaded from NOAA Monthly Isopycnal Mixed-layer Ocean Climatology (MIMOC) (Schmidtko et al., 2013). These maps are constructed using CTD data from Argo floats supplemented with ice-tethered and shipboard profiles. These data were re-gridded to 9 km and binned into seasonal composites to match the temporal and spatial resolution of the satellite data.

2.3 Model development

2.3.1 Existing model

Building on the work by Morel and Berthon (1989), Uitz et al. (2006) developed a model through the statistical analysis of 2,419 profiles across the global oceans that estimates C_{int} (down to $1.5 \times Z_p$) from C_{surf}. The model developed by Uitz et al. (2006) uses a power function such that

$$C_{int} = \alpha {C_{surf}}^{\beta}, \tag{1}$$

where α and β are empirical parameters relating C_{surf} to C_{int}. In the approach used by Uitz et al. (2006), three sets of parameters are provided, depending on whether the waters were deemed mixed or stratified, with the latter category partitioned into low and high Chl-*a* concentrations. To determine whether the waters were mixed or stratified, they used the ratio of Z_p to Z_m. When Z_p/Z_m was greater than or equal to 1, waters were deemed stratified, and when less than 1, mixed. For stratified conditions, low and high Chl-*a* concentrations were separated on either side of 1 mg m^{-3} C_{surf}. Specifically, where $Z_p/Z_m < 1$, $\alpha = 58.5$ and $\beta = 0.546$; where $Z_p/Z_m \geq 1$ and $C_{surf} \leq 1$, $\alpha = 42.0$ and $\beta = 0.248$; and where $Z_p/Z_m \geq 1$ and $C_{surf} > 1$, $\alpha = 43.5$, and $\beta = 0.847$.

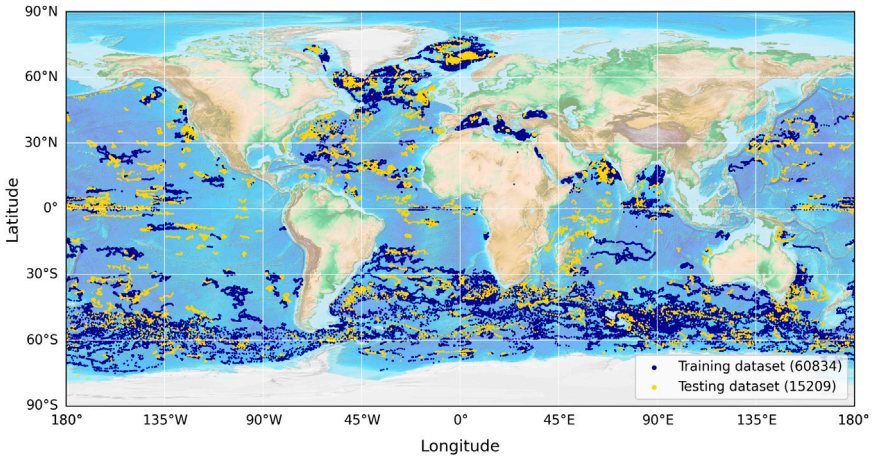

FIGURE 1
Distribution of the data used in this study, obtained from the global BGC-Argo dataset. A total of 76,043 data points were used, split by time into training (blue) and testing (yellow) datasets for model evaluation. The training dataset begins on 30/05/2010 and ends on 21/04/2022, with the testing dataset continuing on and ending on 27/11/2023.

2.3.2 New model

The empirical model developed by Uitz et al. (2006) has proven a useful tool for approximating the stock of Chl-*a* in the euphotic zone from satellite data (e.g., Hatton et al., 2021). However, the model classifies the ocean into binary physical environments, mixed and stratified waters, and further classifies stratified environments into binary trophic levels. In reality, the ocean may not adhere to such a binary classification. Additionally, although based on a two-parameter model (Equation 1), it really requires six parameters to operate over the full range of conditions. Here, building on the approach used by Uitz et al. (2006), we adapt their model to operate continuously over the full range of physical conditions and trophic levels in the ocean while reducing the number of parameters required, thus potentially providing a more parsimonious solution.

We begin by selecting a different but compatible variable to Z_p/Z_m used by Uitz et al. (2006) by computing the optical mixed-layer depth (K_{zm}), estimated as the product of K_d and Z_m. We select this variable instead of Z_p/Z_m due to its relevance with satellite remote sensing since K_d (as a key apparent optical property) can be related more directly to the remote sensing reflectance measured from a satellite. However, it is worth noting that as Z_p/Z_m tends to 1, K_{zm} can be related to Z_p/Z_m according to

$$K_{zm} = \frac{4.6}{Z_p/Z_m}. \tag{2}$$

Next, we model C_{int} (down to 1.5 × Z_p) as a function of C_{surf} and K_{zm} according to

$$C_{int} = \alpha {C_{surf}}^{\beta} + \frac{\gamma\epsilon\left[1/K_{zm}\right]}{\gamma + \epsilon\left[1/K_{zm}\right]}. \tag{3}$$

This model has four parameters, α, β, γ, and ϵ, rather than the six needed in the method used by Uitz et al. (2006). The parameters α and β are equivalent to those used by Uitz et al. (2006) when $1/K_{zm}$ (and the term on the far right side of the equation) tends to 0 (fully mixed water column). As $1/K_{zm}$ increases, the term on the far right side of the equation increases, controlled by the parameter ϵ (slope of increase), until it reaches saturation, which is required to prevent the term from getting too large (reaching a maximum as defined by γ) at very high stratification. Note that the right-hand term was modelled using a Michaelis–Menten style equation, but other similar functions (e.g., saturated exponential) could have been used with a similar effect. Unlike the approach used by Uitz et al. (2006), Equation 3 is applicable in a continuous form to the full range of physical conditions and trophic levels in the ocean. Note that as Z_p/Z_m tends to 1, Equation 2 can be substituted into Equation 3, and the model can be expressed as

$$C_{int} = \alpha {C_{surf}}^{\beta} + \frac{\gamma\epsilon\left[1\Big/\left(\frac{4.6}{Z_p/Z_m}\right)\right]}{\gamma + \epsilon\left[1\Big/\left(\frac{4.6}{Z_p/Z_m}\right)\right]}. \tag{4}$$

2.4 Fitting and evaluating models using the global dataset

To tune and test the method used by Uitz et al. (2006) and the new model (Equation 3), the global dataset was split by time (pre- and post-21 April 2022) into a training and testing dataset (~80–20 split; 60,834–15,209 profiles), both of which were globally representative (Figure 1). We split the data according to time to ensure that the two datasets were independent (Stock and Subramaniam, 2020). Both the method used by Uitz et al. (2006) and the new model (Equation 3) were fitted to the data using the Levenberg–Marquardt least-squares method of minimisation that aims to minimise the chi-squared (χ^2) statistical test, reducing the difference between the model and data (Marquardt, 1963). This was implemented through the use of the lmfit-py package (https://pypi.org/project/lmfit/). Both models were fitted to $\log_{10}$-transformed

TABLE 1 Model parameters used and derived in the study. Brackets represent uncertainty in the parameters.

Model	Condition[$]	α	β	γ	ϵ
Original used by Uitz et al. (2006)	M	58.5	0.546	—	—
	S, LC	42.0	0.248	—	—
	S, HC	43.5	0.847	—	—
Tuned Uitz et al. (2006)	M	52.62 (±0.15)	0.630 (±0.002)	—	—
	S, LC	40.06 (±0.22)	0.245 (±0.002)	—	—
	S, HC	50.81 (±0.59)	0.854 (±0.018)	—	—
New model (Equations 3, 4)	NA	46.82 (±0.16)	0.707 (±0.004)	25.2 (±0.3)	40.6 (±0.8)

[$]M, mixed; S = stratified; LC, low-surface Chl-*a* (<1 mg m^{-3}); HC, high-surface Chl-*a* (>1 mg m^{-3}); NA, not applicable.

C_{int} data, owing to the typical log-normal distribution of Chl-*a* (Campbell, 1995). Model parameters and their uncertainties are given in Table 1.

A number of statistical tests were used to evaluate model performance (e.g., Equations 5, 6). This statistical evaluation was completed on both the training and testing datasets. All statistical evaluations were conducted on C_{int} data following logarithmic (base 10) transformation. The statistical tests included (1) Spearman's rank correlation coefficient (r), chosen to indicate how well the model can explain variance in the data (Python package *scipy. stats*); (2) root mean squared difference (RMSD), which provides an aggregate measure of the magnitude of predicted differences (a single summary statistic that represents the overall difference between the model and data). This was computed as

$$\mathrm{RMSD} = \left[\frac{1}{N}\sum_{i=1}^{N}\left(X_{i,1} - X_{i,2}\right)^2\right]^{1/2}, \tag{5}$$

where X is the variable and N is the number of samples. The subscripts 1 and 2 represent different estimates of the same variable, with 1 representing the estimated variable and 2, the measured variable; and (3) Akaike information criterion (AIC), which considers the fit of the data and the model's simplicity, was used to generate a relative statistic that can be compared between models, with the lower score representing a better model. This was computed as

$$\mathrm{AIC} = 2\kappa + N \cdot \mathrm{In}\left\{\left[\sum_{i=1}^{N}\left(X_{i,1} - X_{i,2}\right)^2\right]\Big/ N\right\}, \tag{6}$$

where κ is the number of parameters in the model.

2.5 Application of the new model

To illustrate applications of the new model, we simulated the influence of changes in the mixed-layer depth on model simulations of C_{int} and forced our model with seasonal mean climatologies of satellite data on surface Chl-*a* and the diffuse attenuation coefficient (K_d), and MIMOC MLDs, to produce seasonal maps of C_{int}. We also explored the spatial distribution of the term on the far right side of Equation 3, which is directly related to $1/K_{zm}$, and interpreted this term in the context of regions of the ocean with strong vertical gradients in Chl-*a*.

3 Results and discussion

3.1 Existing model results

The original model used by Uitz et al. (2006) (see parameters in Table 1) was found to agree well with the BGC-Argo dataset (Figure 2A). There is a clear division between mixed and stratified waters, and the original regressions capture these broad differences (Figure 2A). This division between mixed and stratified waters essentially reflects the fact that within the euphotic zone when waters are mixed, chlorophyll-*a* is relatively uniform with depth, whereas when conditions stratify, the vertical stricture of chlorophyll-*a* is non-uniform, with the presence of a DCM. Considering that this model was developed using a much smaller, independent dataset (2,419 profiles) with less extensive global coverage (Uitz et al., 2006), it is quite remarkable how well the original concept developed by Morel and Berthon (1989) performs. The model estimates of C_{int} are well-correlated with both training and testing datasets ($r > 0.7$; Table 2), with reasonably low RMSD (<0.2; Table 2).

Re-tuning the model used by Uitz et al. (2006) to the training dataset (Table 1) yielded in a significant increase in performance over the original model (lower RMSD and AIC) compared with the testing dataset (Table 2). However, the new set of parameters was only marginally different from the original ones (Figure 2A; Table 1). Regressions for the three different ranges (mixed, stratified low C_{surf}, and stratified high C_{surf}) were all performed independently (as done by Uitz et al. (2006)). This did create a slight discontinuity at the boundary (1 mg m^{-3}; see Figure 2A) between stratified regressions, with the α parameter differing significantly between low and high C_{surf}, with a wider difference than in the original approach (Table 1). Future work could look to avoid such a discontinuity by having a fixed α parameter for stratified waters and only varying β between low and high C_{surf}, although this may reduce model performance.

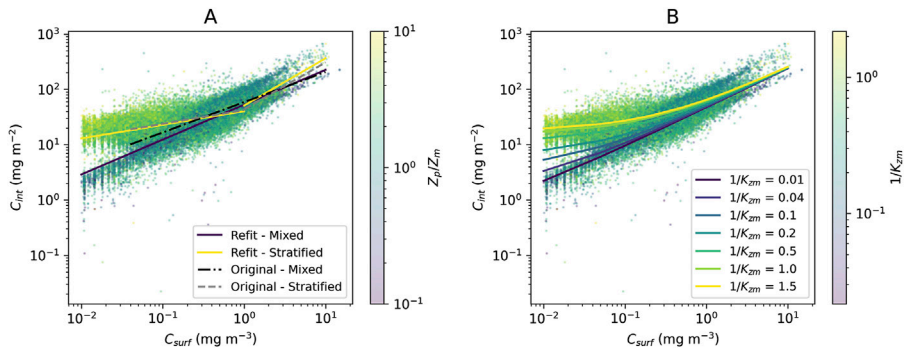

FIGURE 2
(A) Original model used by Uitz et al. (2006) and the refit of the model used by Uitz et al. (2006) to the global BGC-Argo dataset overlain onto the scatter plot of surface vs column-integrated Chl-*a* for the entire dataset (training and testing) with points colour-coded according to the ratio Z_p/Z_m. **(B)** New model overlain onto the scatter plot of surface vs column-integrated Chl-*a* for the entire dataset (training and testing) with points colour-coded according to the ratio $1/K_{zm}$.

TABLE 2 Statistical comparison of models with training and testing datasets.

Model	Dataset	*r**	RMSD*	AIC*	*N*[$]
Original used by Uitz et al. (2006)	Training	0.731	0.180	−208632	60,834
Tuned Uitz et al. (2006)	Training	0.748	0.168	−216821	60,834
New model (Equations 3 and 4)	Training	0.762	0.165	−219462	60,834
Original used by Uitz et al. (2006)	Testing	0.705	0.194	−49831	15,209
Tuned Uitz et al. (2006)	Testing	0.715	0.177	−52595	15,209
New model (Equations 3, 4)	Testing	0.730	0.176	−52769	15,209

[a]All statistical tests performed after log-transformation (base 10) of the data.
[$] *N* refers to the number of samples.

3.2 New model results

Simulations overlain onto the entire BGC-Argo dataset (training and testing; Figure 2B) illustrate how the new model performs in a continuous manner over the full range of C_{surf} and $1/K_{zm}$, without any discontinuities or any binary switch between mixed and stratified conditions. It appears to capture the change in C_{int}, for a similar low C_{surf}, as the environment moves from well-mixed ($1/K_{zm} < 0.2$) to more stratified conditions ($1/K_{zm} \geq 0.2$).

The α and β parameters derived from the training dataset for the new model (Equations 3, 4) were found to lie around the mid-range of those of the tuned model used by Uitz et al. (2006) for the different environments (Table 1). Parameters for the right-hand term of Equation 3 are given in Table 2, and the term is plotted as a function of $1/K_{zm}$ in Figure 3A, where it is seen to initially increase as a linear function of $1/K_{zm}$, according to ϵ, until it reaches a half-saturation (γ/ϵ) point beyond which the term begins to saturate, with a theoretical limit represented by γ.

Compared with the re-tuned and original models used by Uitz et al. (2006), the new model has a similar performance in both the training and testing datasets (Table 2), albeit with a slightly higher correlation coefficient and lower RMSD and AIC. Although these improvements are small, when considering how large the datasets are, improvements are significant, for example, the increase in the correlation coefficient in both training and testing datasets (Table 2, Z-test, $p < 0.05$). Considering that the new model has a lower number of parameters [four compared with the six used by Uitz et al. (2006)], it can also be considered a more parsimonious model, as partly reflected by a lower AIC.

3.3 Changes in vertical structure with increasing stratification

The term on the far right-hand side of Equation 3 ($\frac{\gamma\epsilon[1/K_{zm}]}{\gamma+\epsilon[1/K_{zm}]}$), shown in Figure 3A, essentially reflects non-uniform changes in the vertical structure of Chl-*a* with increasing stratification ($1/K_{zm}$). As the waters become more stratified, a deep Chl-*a* maximum forms, increasing Chl-*a* at depth relative to its surface values. DCMs can occur from an increase in biomass at depth (typical of high-latitude, seasonally stratified regions), or due to the physiological changes in the phytoplankton, where the cells in different parts of the water column increase (or decrease) their Chl-*a* concentration in response to decreasing (increasing) light levels, without changing their biomass (e.g., carbon concentration) (Cullen, 2015).

To investigate drivers of the right-hand term of Equation 3, we plotted surface particle backscattering ($b_{bp,surf}$) against column-integrated particle backscattering ($b_{bp,\mathrm{int}}$) (Figure 3B).

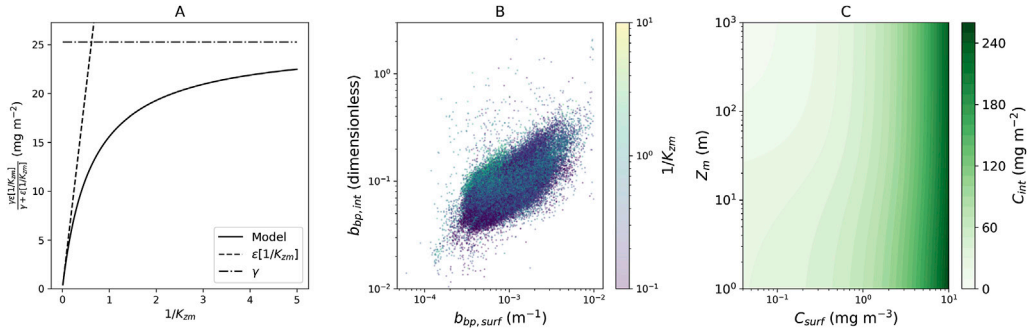

FIGURE 3
(A) Relationship between the term on the far right-hand side of Equation 3 ($\frac{\gamma\epsilon[1/K_{zm}]}{\gamma+\epsilon[1/K_{zm}]}$) and $1/K_{zm}$. **(B)** Relationship between $b_{bp,surf}$ and $b_{bp,int}$ for the entire dataset (training and testing), with points colour-coded according to the ratio $1/K_{zm}$. **(C)** Model simulations of C_{int} as a function of C_{surf} (tied to K_d, following Morel et al. (2007)) and mixed-layer depth (Z_m).

Phytoplankton carbon and light-scattering properties of particles (including b_{bp}) are correlated with each other over a range of scales (Behrenfeld et al., 2005; Martinez-Vicente et al., 2013; Graff et al., 2015). Unlike for Chl-*a* (Figure 2), there are no clear differences in the relationships for b_{bp} between stratified and mixed waters (Figure 3B). Considering that these relationships are less evident in b_{bp} (by proxy phytoplankton carbon), it is likely that changes in the carbon-to-Chl-*a* ratio is an important driver of the term on the far right-hand side of Equation 3. This change may be occurring at the DCM (increase in Chl-*a* at low light, often referred to as a deep acclimation maximum; Cornec et al., 2021) and/or at the surface (decrease in Chl-a at high light; Brewin et al., 2022) and could be driven by photoacclimation and/or shifts in the phytoplankton community structure (Viljoen et al., 2024).

3.4 Model applications

The new model could provide a useful, empirical constraint on future predictions on shifts in the vertical structure of Chl-*a* in the open ocean in a changing climate. To illustrate this, we simulated (Figure 3C) C_{int} for varying C_{surf} and mixed-layer depths (Z_m), tying K_d to C_{surf}, following Morel et al. (2007) (case I assumption is that phytoplankton control optical properties in the open ocean). The model simulations indicate that in lower C_{surf} waters, as the mixed-layer shoals, there is a substantial increase in C_{int} for the same C_{surf} (Figure 3C). Such simulations may not only provide an insight into how the vertical structure in Chl-*a* could be impacted by a shoaling (or deepening) of Z_m but also show that we should be cautious when using satellite measurements of C_{surf} for interpreting C_{int} without information about Z_m.

Figure 4 shows the seasonal estimates of global C_{int} derived from satellite climatologies on C_{surf} and K_d and MIMOC Z_m climatologies. C_{int} shows large blooms visible north of 50 °N in the boreal spring and summer (March–May and June–August) and similar blooms in the Southern Hemisphere (SH) during austral spring and summer (September–November and December–February). High C_{int} is also observed in coastal waters and upwelling zones. Oligotrophic regions (low C_{int}) are also identifiable as the large tropical ocean gyres in the Atlantic, Pacific, and Indian oceans.

Spatial maps of the far right-hand term of Equation 3 (Figure 4) also provide an insight into regions that exhibit strong vertical gradients in Chl-*a*. The term contributes more significantly in sub-tropical regions but displays temporal variability in seasonal stratified high-latitude regions. Collectively, these images demonstrate how the new model can be used with satellite data and Z_m information to study spatial and temporal variability in C_{int} and help identify regions of the ocean with strong vertical gradients in Chl-*a*.

3.5 Potential limitations to our study and future perspectives

Morel and Berthon (1989) and Uitz et al. (2006) used discrete measurements of extracted Chl-*a* (either using fluorescence or high-performance liquid chromatography), as opposed to this study that used less accurate *in vivo* estimates of Chl-*a*, only available on BGC-Argo floats. For the same Chl-*a* concentration, variations in the *in vivo* fluorescence signal can occur with species composition and physiological status, impacting conversion factors (see the study by Petit et al., 2022), especially in the Southern Ocean (Schallenberg et al., 2022). There are also uncertainties in the non-photochemical quenching correction used in BGC-Argo data processing (Schmechtig et al., 2023).

Uncertainties also exist for other variables used in the model. For example, for many profiles, PAR data were not available, so K_d was estimated empirically (Morel et al., 2007). To harness the power of BGC-Argo floats, continued efforts are needed to develop rigorous, community-agreed protocols, quantify measurement uncertainties, and ensure that a standard set of key ocean variables are collected (Claustre et al., 2020). The equations used in this study are empirical in nature. Thus, they do not solve for detailed changes in the vertical structure in Chl-*a* and, so, are somewhat limited in applications. To do that, other empirical approaches are required (e.g., Brewin et al., 2022) or more mechanistic ecosystem modelling (IOCCG, 2020).

With the climate changing rapidly, it is important to have tools to provide accurate estimations of the phytoplankton stock and physiology in the global oceans and ensure relevant monitoring of spatial and temporal changes. By developing simple models that can

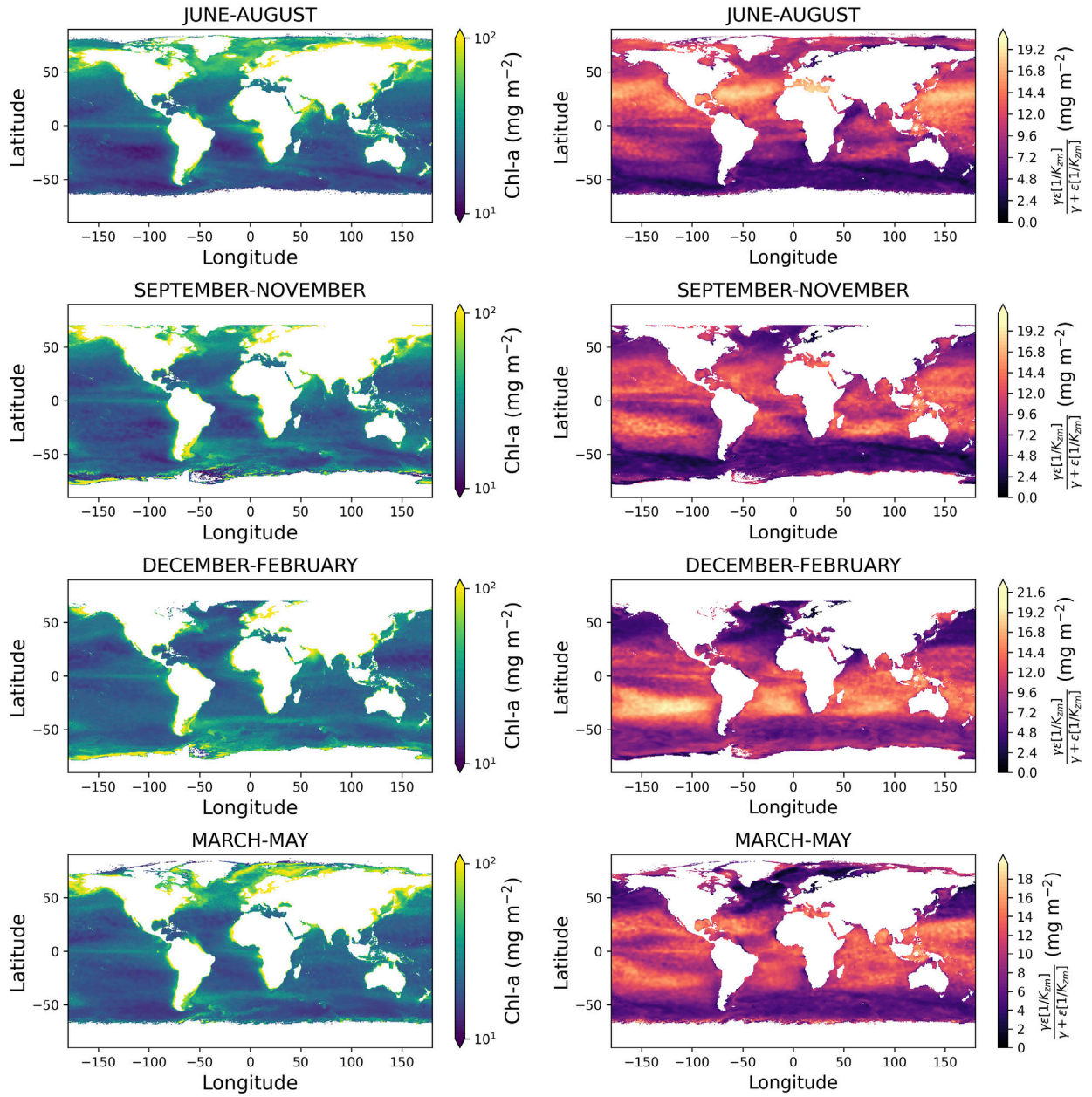

FIGURE 4
Left column shows global maps of estimated column-integrated Chl-*a* (C_{int}) in the euphotic zone for the four seasons, derived from Equation 3 using global satellite estimates of C_{surf}, K_d, and maps of Z_m. The right column shows the contribution from the far right-hand term of Equation 3 ($\frac{\gamma\epsilon[1/K_{zm}]}{\gamma+\epsilon[1/K_{zm}]}$) to C_{int} for the four seasons.

combine the benefits of high-spatial and temporal observation of the surface ocean by satellites, with the vertical profiling of autonomous platforms, we can improve the way we quantify changes in phytoplankton stock and physiology. Moving forward, it will be important to continue tuning the model as more data become available. It may also be fruitful to apply the model to specific regions with unique characteristics where the parameters may differ, for example, in Arctic waters (Ardyna et al., 2013) and the Mediterranean Sea (Li et al., 2022).

3.6 Summary

Using a global array of BGC-Argo floats (76,043 profiles, spanning from 2010 to 2023), we re-evaluated empirical relationships between the surface and column-integrated concentrations of Chl-*a* developed by Morel and Berthon (1989) and extended by Uitz et al. (2006). We found that these relationships agree well with BGC-Argo float data. The relationships were then extended so that the column-integrated Chl-*a* concentration could be estimated as a continuous function of its surface

value and a proxy for stratification (optical mixed-layer depth) without the need for a binary switch in parameters between mixed and stratified waters. The extended model has fewer parameters and performed better in statistical tests than earlier models. Applications of the new model include studying the impact of increasing stratification on the relationship between surface and column-integrated concentrations of Chl-*a*, using satellite data for monitoring spatial and temporal variations in column-integrated concentrations of Chl-*a,* and identifying and monitoring regions of the ocean with strong vertical gradients in Chl-*a*.

Data availability statement

The original contributions presented in the study are included in the article; further inquiries can be directed to the corresponding author.

Author contributions

ET: formal analysis, funding acquisition, investigation, methodology, resources, software, validation, visualization, and writing–original draft. HE: formal analysis, investigation, visualization, and writing–review and editing. JV: methodology, resources, software, and writing–review and editing. RB: conceptualization, formal analysis, funding acquisition, investigation, methodology, project administration, resources, software, supervision, validation, visualization, writing–original draft, and writing–review and editing.

Funding

The author(s) declare that financial support was received for the research, authorship, and/or publication of this article. RB and JV were funded by a UKRI Future Leader Fellowship (MR/V022792/1). ET was supported by two Engineering and Physical Sciences Research Council summer internships.

Acknowledgments

ET and HE were supported by the B.Sc programme in Environmental Science at the University of Exeter Cornwall. The authors thank all those who contributed to the acquisition and processing of BGC-Argo data. The authors also thank NASA for providing the global MODIS-Aqua data and NOAA for global mixed-layer depths. BGC-Argo data used were collected and made freely available by the International Argo Program and the national programs that contribute to it (https://argo.ucsd.edu, https://www.ocean-ops.org). The Argo Program is part of the Global Ocean Observing System. Satellite data used are freely available on the NASA website (https://oceancolor.gsfc.nasa.gov). Mixed layer depth climatologies used are freely available on the NOAA website (https://www.pmel.noaa.gov/mimoc/). For the purpose of open access, the author has applied a Creative Commons Attribution (CC BY) licence to any Author Accepted Manuscript version arising from this submission.

Conflict of interest

The authors declare that the research was conducted in the absence of any commercial or financial relationships that could be construed as a potential conflict of interest.

The reviewer EC declared a past co-authorship with the author RB to the handling Editor.

Publisher's note

References

Ardyna, M., Babin, M., Gosselin, M., Devred, E., Bélanger, S., Matsuoka, A., et al. (2013). Parameterization of vertical chlorophyll a in the Arctic Ocean: impact of the subsurface chlorophyll maximum on regional, seasonal, and annual primary production estimates. *Biogeosciences* 10, 4383–4404. doi:10.5194/bg-10-4383-2013

Ardyna, M., Babin, M., Gosselin, M., Devred, E., Rainville, L., and Tremblay, J. (2014). Recent Arctic ocean sea ice loss triggers novel fall phytoplankton blooms. *Geophys. Res. Lett.* 41, 6207–6212. doi:10.1002/2014GL061047

Ardyna, M., Claustre, H., Sallée, J., D'Ovidio, F., Gentili, B., van Dijken, G., et al. (2017). Delineating environmental control of phytoplankton biomass and phenology in the Southern Ocean. *Geophys. Res. Lett.* 44, 5016–5024. doi:10.1002/2016GL072428

Barnes, C., Maxwell, D., Reuman, D. C., and Jennings, S. (2010). Global patterns in predator–prey size relationships reveal size dependency of trophic transfer efficiency. *Ecology* 91, 222–232. doi:10.1890/08-2061.1

Bazzani, E., Lauritano, C., and Saggiomo, M. (2023). Southern Ocean iron limitation of primary production between past knowledge and future projections. *J. Mar. Sci. Eng.* 11, 272. doi:10.3390/jmse11020272

Behrenfeld, M. J., Boss, E., Siegel, D. A., and Shea, D. M. (2005). Carbon-based ocean productivity and phytoplankton physiology from space. *Glob. Biogeochem. Cycles* 19. doi:10.1029/2004GB002299

Bittig, H. C., Maurer, T. L., Plant, J. N., Schmechtig, C., Wong, A. P. S., Claustre, H., et al. (2019). A BGC-Argo guide: planning, deployment, data handling and usage. *Front. Mar. Sci.* 6. doi:10.3389/fmars.2019.00502

Boyd, P., Claustre, H., Levy, M., Siegel, D., and Weber, T. (2019). Multi-faceted particle pumps drive carbon sequestration in the ocean. *Nature* 568, 327–335. doi:10.1038/s41586-019-1098-2

Brewin, R. J. W., Dall'Olmo, G., Gittings, J., Sun, X., Lange, P. K., Raitsos, D. E., et al. (2022). A conceptual approach to partitioning a vertical profile of phytoplankton biomass into contributions from two communities. *J. Geophys. Res. Oceans* 127, e2021JC018195. doi:10.1029/2021JC018195

Cael, B., Bisson, K., Boss, E., Dutkiewicz, S., and Henson, S. (2023). Global climate-change trends detected in indicators of ocean ecology. *Nature* 619, 551–554. doi:10.1038/s41586-023-06321-z

Campbell, J. W. (1995). The lognormal distribution as a model for bio-optical variability in the sea. *J. Geophys. Res. Oceans* 100, 13237–13254. doi:10.1029/95JC00458

Chai, F., Johnson, K. S., Claustre, H., Xing, X., Wang, Y., Boss, E., et al. (2020). Monitoring ocean biogeochemistry with autonomous platforms. *Nat. Rev. Earth and Environ.* 1, 315–326. doi:10.1038/s43017-020-0053-y

Cheng, L., Abraham, J., Hausfather, Z., and Trenberth, K. E. (2019). How fast are the oceans warming? *Science* 363, 128–129. doi:10.1126/science.aav7619

Claustre, H., Johnson, K. S., and Takeshita, Y. (2020). Observing the global ocean with Biogeochemical-Argo. *Annu. Rev. Mar. Sci.* 12, 23–48. doi:10.1146/annurev-marine-010419-010956

Cornec, M., Claustre, H., Mignot, A., Guidi, L., Lacour, L., Poteau, A., et al. (2021). Deep chlorophyll maxima in the Global Ocean: occurrences, drivers and characteristics. *Glob. Biogeochem. Cycles* 35, e2020GB006759. doi:10.1029/2020GB006759

Cox, I., Brewin, R. J. W., Dall'Olmo, G., Sheen, K., Sathyendranath, S., Rasse, R., et al. (2023). Distinct habitat and biogeochemical properties of low-oxygen-adapted tropical oceanic phytoplankton. *Limnol. Oceanogr.* 68, 2022–2039. doi:10.1002/lno.12404

Cullen, J. J. (2015). Subsurface chlorophyll maximum layers: enduring enigma or mystery solved? *Annu. Rev. Mar. Sci.* 7, 207–239. doi:10.1146/annurev-marine-010213-135111

Dai, Y., Yang, S., Zhao, D., Hu, C., Xu, W., Anderson, D. M., et al. (2023). Coastal phytoplankton blooms expand and intensify in the 21st century. *Nature* 615, 280–284. doi:10.1038/s41586-023-05760-y

Boyer Montégut, C., Madec, G., Fischer, A. S., Lazar, A., and Iudicone, D. (2004). Mixed layer depth over the global ocean: an examination of profile data and a profile-based climatology. *J. Geophys. Res. Oceans* 109. doi:10.1029/2004JC002378

Deppeler, S. L., and Davidson, A. T. (2017). Southern Ocean phytoplankton in a changing climate. *Front. Mar. Sci.* 4. doi:10.3389/fmars.2017.00040

Falkowski, P. G. (1994). The role of phytoplankton photosynthesis in global biogeochemical cycles. *Photosynth. Res.* 39, 235–258. doi:10.1007/BF00014586

Falkowski, P. G., Laws, E. A., Barber, R. T., and Murray, J. W. (2003). *Phytoplankton and their role in primary, new, and export production*. Berlin, Heidelberg: Springer Berlin Heidelberg, 99–121. doi:10.1007/978-3-642-55844-3_5

Ferreira, A., Dias, J., Brotas, V., and Brito, A. C. (2022). A perfect storm: an anomalous offshore phytoplankton bloom event in the NE Atlantic (March 2009). *Sci. Total Environ.* 806, 151253. doi:10.1016/j.scitotenv.2021.151253

Field, C., Behrenfeld, M., Randerson, J., and Falkowski, P. (1998). Primary production of the biosphere: integrating terrestrial and oceanic components. *Science* 281, 237–240. doi:10.1126/science.281.5374.237

Garnesson, P., Mangin, A., Fanton d'Andon, O., Demaria, J., and Bretagnon, M. (2019). The CMEMS Globcolour chlorophyll a product based on satellite observation: multi-sensor merging and flagging strategies. *Ocean Sci.* 15, 819–830. doi:10.5194/os-15-819-2019

Gould, J., Sloyan, B., and Visbeck, M. (2013). "Chapter 3 - *in situ* Ocean Observations: a brief history, present status, and future directions," in *Ocean Circulation and climate - a 21st century perspective (elsevier)*, 59–81. doi:10.1016/B978-0-12-391851-2.00003-9

Graff, J. R., Westberry, T. K., Milligan, A. J., Brown, M. B., Dall'Olmo, G., van Dongen-Vogels, V., et al. (2015). Analytical phytoplankton carbon measurements spanning diverse ecosystems. *Deep Sea Res. Part I Oceanogr. Res. Pap.* 102, 16–25. doi:10.1016/j.dsr.2015.04.006

Groom, S., Sathyendranath, S., Ban, Y., Bernard, S., Brewin, R., Brotas, V., et al. (2019). Satellite ocean colour: current status and future perspective. *Front. Mar. Sci.* 6, 1–30. doi:10.3389/fmars.2019.00485

Hatton, I., Heneghan, R., Bar-On, Y., and Galbraith, E. (2021). The global ocean size-spectrum from bacteria to whales. *Sci. Adv.* 7, eabh3732. doi:10.1126/sciadv.abh3732

IOCCG (2020). Synergy between ocean colour and biogeochemical/ecosystem models. Tech. Rep in *IOCCG report series, No. 19, international ocean colour coordinating group, dartmouth, Canada*.

IPCC (2021). *Climate change 2021: the physical science basis. Contribution of working group I to the sixth assessment report of the intergovernmental panel on climate change*. Cambridge: Cambridge University Press. doi:10.1017/9781009157896

Jayne, S. R., Roemmich, D., Zilberman, N., Riser, S., Johnson, K., Johnson, G., et al. (2017). The argo program: present and future. *Oceanography* 30, 18–28. doi:10.5670/oceanog.2017.213

Kiørboe, T. (1993). Turbulence, phytoplankton cell size, and the structure of pelagic food webs. *Adv. Mar. Biol. (Elsevier)* 29, 1–72. doi:10.1016/S0065-2881(08)60129-7

Lalli, C., and Parsons, T. R. (1997). *Biological oceanography: an introduction*. Elsevier.

Legendre, L., and Rassoulzadgan, F. (1996). Food-web mediated export of biogenic carbon in oceans: hydrodynamic control. *Mar. Ecol. Prog. Ser.* 145, 179–193. doi:10.3354/meps145179

Le Moigne, F., Boye, M., Masson, A., Corvaisier, R., Grossteffan, E., Pondaven, P., et al. (2013). Description of the biogeochemical features of the subtropical southeastern Atlantic and the Southern Ocean south of South Africa during the austral summer of the International Polar Year. *Biogeosciences* 10, 281–295. doi:10.5194/bg-10-281-2013

Le Traon, P.-Y., Antoine, D., Bentamy, B.-H. A., Breivik, L., Chapron, B., Corlett, G., et al. (2015). Use of satellite observations for operational oceanography: recent achievements and future prospects. *J. Operational Oceanogr.* 8, s12–s27. doi:10.1080/1755876X.2015.1022050

Li, X., Mao, Z., Zheng, H., Zhang, W., Yuan, D., Li, Y., et al. (2022). Process-oriented estimation of chlorophyll-a vertical profile in the Mediterranean Sea using MODIS and oceanographic float products. *Front. Mar. Sci.* 9. doi:10.3389/fmars.2022.933680

Longhurst, A., Sathyendranath, S., Platt, T., and Caverhill, C. (1995). An estimate of global primary production in the ocean from satellite radiometer data. *J. Plankton Res.* 17, 1245–1271. doi:10.1093/plankt/17.6.1245

Lu, W., Gao, X., Wu, Z., Wang, T., Lin, S., Xiao, C., et al. (2022). Framework to extract extreme phytoplankton bloom events with remote sensing datasets: a case study. *Remote Sens.* 14, 3557. doi:10.3390/rs14153557

Ma, L., Bai, X., Laws, E. A., Xiao, W., Guo, C., Liu, X., et al. (2023). Responses of phytoplankton communities to internal waves in oligotrophic oceans. *J. Geophys. Res. Oceans* 128, e2023JC020201. doi:10.1029/2023jc020201

Marquardt, D. (1963). An algorithm for least-squares estimation of nonlinear parameters. *J. Soc. Industrial Appl. Math.* 11, 431–441. doi:10.1137/0111030

Martinez-Vicente, V., Dall'Olmo, G., Tarran, G., Boss, E., and Sathyendranath, S. (2013). Optical backscattering is correlated with phytoplankton carbon across the Atlantic Ocean. *Geophys. Res. Lett.* 40, 1154–1158. doi:10.1002/grl.50252

McClain, F.-G. H. S. C., Feldman, G. C., and Hooker, S. B. (2004). An overview of the SeaWiFS project and strategies for producing a climate research quality global ocean bio-optical time series. *Deep Sea Res. Part II Top. Stud. Oceanogr.* 51, 5–42. doi:10.1016/j.dsr2.2003.11.001

Mignot, A., Claustre, H., Uitz, J., Poteau, A., D'Ortenzio, F., and Xing, X. (2014). Understanding the seasonal dynamics of phytoplankton biomass and the deep chlorophyll maximum in oligotrophic environments: a bio-argo float investigation. *Glob. Biogeochem. Cycles* 28, 856–876. doi:10.1002/2013gb004781

Miller, C. (2004). *Biological oceanography*. Oxford: Blackwell Publishing.

Morel, A., and Berthon, J.-F. (1989). Surface pigments, algal biomass profiles, and potential production of the euphotic layer: relationships reinvestigated in view of remote-sensing applications. *Limnol. Oceanogr.* 34, 1545–1562. doi:10.4319/lo.1989.34.8.1545

Morel, A., Huot, Y., Gentili, B., Werdell, P., Hooker, S., and Franz, B. (2007). Examining the consistency of products derived from various ocean color sensors in open ocean (case 1) waters in the perspective of a multi-sensor approach. *Remote Sens. Environ.* 111, 69–88. doi:10.1016/j.rse.2007.03.012

NASA (2022). NASA goddard space flight center, ocean ecology laboratory, ocean biology processing group in *Moderate-resolution imaging spectroradiometer (MODIS) Aqua CHL data*. Greenbelt: NASA OB.DAAC. doi:10.5067/AQUA/MODIS/L3M/CHL/2022

Nowicki, M., DeVries, T., and Siegel, D. (2022). Quantifying the carbon export and sequestration pathways of the ocean's biological carbon pump. *Glob. Biogeochem. Cycles* 36, e2021GB007083. doi:10.1029/2021gb007083

Oka, R., Talley, L., and Suga, T. (2007). Temporal variability of winter mixed layer in the mid-to high-latitude North Pacific. *J. Oceanogr.* 63, 293–307. doi:10.1007/s10872-007-0029-2

Petit, F., Uitz, J., Schmechtig, C., Dimier, C., Ras, J., Poteau, A., et al. (2022). Influence of the phytoplankton community composition on the *in situ* fluorescence signal: implication for an improved estimation of the chlorophyll-a concentration from biogeochemical-argo profiling floats. *Front. Mar. Sci.* 9. doi:10.3389/fmars.2022.959131

Roemmich, D., Johnson, G., Riser, S., Davis, R., Gilson, J., Owens, W., et al. (2009). The argo program: observing the global oceans with profiling floats. *Oceanography* 22, 34–43. doi:10.5670/oceanog.2009.36

Schallenberg, C., Strzepek, R. F., Bestley, S., Wojtasiewicz, B., and Trull, T. W. (2022). Iron limitation drives the globally extreme fluorescence/chlorophyll ratios of the Southern Ocean. *Geophys. Res. Lett.* 49, e2021GL097616. doi:10.1029/2021GL097616

Schmechtig, C., Claustre, H., Poteau, A., D'Ortenzio, F., Schallenberg, C., Trull, T., et al. (2023). *BGC-Argo quality control manual for the Chlorophyll-a concentration*. doi:10.13155/35385

Schmidtko, S., Johnson, G. C., and Lyman, J. M. (2013). MIMOC: a global monthly isopycnal upper-ocean climatology with mixed layers. *J. Geophys. Res. Oceans* 118, 1658–1672. doi:10.1002/jgrc.20122

Sergi, S., Baudena, A., Cotte, C., Ardyna, M., Blain, S., and d'Ovidio, F. (2020). Interaction of the Antarctic circumpolar current with seamounts fuels moderate blooms but vast foraging grounds for multiple marine predators. *Front. Mar. Sci.* 7. doi:10.3389/fmars.2020.00416

Sridevi, B., Srinivasu, K., Bhavani, T., and Prasad, K. (2019). Extreme events enhance phytoplankton bloom in the south-western Bay of Bengal. *Indian J. Geo Mar. Sci.* 48, 253–258.

Stock, A., and Subramaniam, A. (2020). Accuracy of empirical satellite algorithms for mapping phytoplankton diagnostic pigments in the open ocean: a supervised learning perspective. *Front. Mar. Sci.* 7. doi:10.3389/fmars.2020.00599

Strzedek, R., Boyd, P., and Sunda, W. (2019). Photosynthetic adaptation to low iron, light, and temperature in Southern Ocean phytoplankton. *Proc. Natl. Acad. Sci.* 116, 4388–4393. doi:10.1073/pnas.1810886116

Trainer, V., Moore, S., Hallegraeff, G., Kudela, R., Clement, A., Mardones, J., et al. (2020). Pelagic harmful algal blooms and climate change: lessons from nature's experiments with extremes. *Harmful Algae* 91, 101591. doi:10.1016/j.hal.2019.03.009

Uitz, J., Claustre, H., Morel, A., and Hooker, S. (2006). Vertical distribution of phytoplankton communities in open ocean: an assessment based on surface chlorophyll. *J. Geophys. Res. Oceans* 111. doi:10.1029/2005jc003207

Viljoen, J. V., Sun, X., and Brewin, R. J. W. (2024). Climate variability shifts the vertical structure of phytoplankton in the Sargasso Sea. *Nat. Clim. Change*. doi:10.1038/s41558-024-02136-6

Wang, Y., Chen, H.-H., Tang, R., He, D., Lee, Z., Xue, H., et al. (2022). Australian fire nourishes ocean phytoplankton bloom. *Sci. Total Environ.* 807, 150775. doi:10.1016/j.scitotenv.2021.150775

Wang, Y., Liu, D., Xiao, W., Zhou, P., Tian, C., Zhang, C., et al. (2021). Coastal eutrophication in China: trend, sources, and ecological effects. *Harmful Algae* 107, 102058. doi:10.1016/j.hal.2021.102058

Xiao, W., Liu, X., Irwin, A. J., Laws, E. A., Wang, L., Chen, B., et al. (2018). Warming and eutrophication combine to restructure diatoms and dinoflagellates. *Water Res.* 128, 206–216. doi:10.1016/j.watres.2017.10.051